

# Optical spectroscopy of the low mass X-ray binary GX 9+9

R. Cornelisse<sup>1,2\*</sup>, D. Steeghs<sup>3,4</sup>, J. Casares<sup>1</sup>, P.A. Charles<sup>5,2</sup>, A.D. Barnes<sup>2</sup>,  
R.I. Hynes<sup>6</sup>, K. O’Brien<sup>7</sup>

<sup>1</sup>*Instituto de Astrofísica de Canarias, Via Lactea, La Laguna E-38200, Santa Cruz de Tenerife, Spain*

<sup>2</sup>*School of Physics and Astronomy, University of Southampton, Highfield, Southampton SO17 1BJ, UK*

<sup>3</sup>*Harvard-Smithsonian Center for Astrophysics, 60 Garden Street, Cambridge, MA 02138, USA*

<sup>4</sup>*Department of Physics, University of Warwick, Coventry, CV4 7AL, UK*

<sup>5</sup>*South Africa Astronomical Observatory, P.O.Box 9.Observatory 7935, South Africa*

<sup>6</sup>*Department of Physics and Astronomy, 202 Nicholson Hall, Louisiana State University, Baton Rouge, LA 70803, USA*

<sup>7</sup>*European Southern Observatory, Casilla 19001, Santiago 19, Chile*

Accepted Received ; in original form

## ABSTRACT

Phase-resolved medium resolution VLT spectroscopy of the low mass X-ray binary GX 9+9 has revealed narrow C III emission lines that move in phase relative to our new estimate of the ephemeris, and show a velocity amplitude of  $230 \pm 35 \text{ km s}^{-1}$ . We identify the origin of these lines as coming from the surface of the donor star, thereby providing the first estimate of the mass function of  $f(M_1) \geq 0.22 M_\odot$ . Rotational broadening estimates together with assumptions for the mass donor give  $0.07 \leq q \leq 0.35$  and  $182 \leq K_2 \leq 406 \text{ km s}^{-1}$ . Despite a low mass ratio, there is no evidence for a superhump in our dataset. Doppler maps of GX 9+9 show the presence of a stream overflow, either in the form of material flowing downward along the accretion disk rim or in a similar fashion as occurs in high mass transfer rate cataclysmic variables known as the SW Sex stars. Finally we note that the Bowen region in GX 9+9 is dominated by C III instead of N III emission as has been the case for most other X-ray binaries.

**Key words:** accretion, accretion disks – stars:individual (GX 9+9) – X-rays:binaries.

## 1 INTRODUCTION

One of the main aims of optical observations of low mass X-ray binaries (LMXBs) has always been to find a signature of the donor star, and thereby constrain the masses of both components. However, until recently it was mainly the LMXBs that show transient outbursts for which it was possible to determine the mass function (see e.g. Charles & Coe 2006). During a transient outburst the optical emission is completely dominated by the X-ray irradiated accretion disk, and it is only when the source has returned to quiescence (or at least the X-ray flux has decreased by several orders) that the donor star becomes directly visible. That is why, until recently, there were no strong constraints on the mass of the donor and compact object for most LMXBs that are persistently bright, although optical counterparts have been known for many systems for over 20 years.

This situation changed when Steeghs & Casares (2002) developed a new technique to detect the companion star in persistent LMXBs. Using phase-resolved blue spectroscopy they revealed narrow emission line components that were

interpreted as coming from the irradiated companion star of Sco X-1. This enabled them for the first time to determine the mass function. These narrow features were most obvious in the Bowen blend (a blend of N III 4634/4640 Å and C III 4647/4650 Å lines), which is the result of UV fluorescence due to the hot inner disk for the N III lines or photoionization and subsequent recombination for the C III lines (McClintock et al. 1975). This led to the discovery of such signatures in other persistent LMXBs such as X 1822–371, 4U 1636–53 and 4U 1735–44 (Casares et al. 2003, 2006), or transient sources where the system parameters could not be constrained in quiescence such as GX 339–4 or Aql X-1 (Hynes et al. 2003, Cornelisse et al. 2007).

GX 9+9 is a persistent LMXB that is bright in both optical as well as X-rays and is another good candidate for a Bowen study. Its compact object is thought to be a neutron star due to its X-ray spectral and timing properties (e.g. Hasinger & van der Klis 1989), although direct evidence such as Type I X-ray bursts or pulsations have not been observed thus far. The optical counterpart of GX 9+9 was identified by Davidsen et al. (1976) as a  $V=16.6$  blue object. A 4.2 hour periodic modulation in X-rays was detected that was interpreted as the orbital modulation (Hertz & Wood

\* E-mail: corneli@iac.es

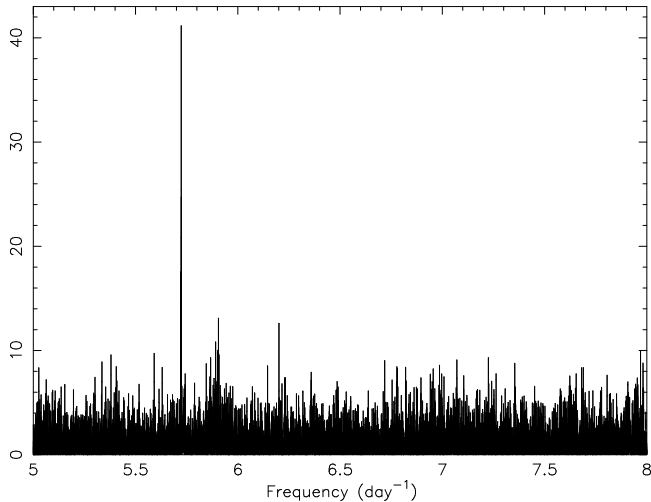


**Figure 1.** Scargle normalised power spectrum of the RXTE/ASM data of GX 9+9, showing a strong peak at the expected (orbital) period of  $\simeq 4.2$  hrs.

1988), and confirmed in the optical by Schaefer (1990). From its aperiodic variability at very low frequencies, Reig et al. (2003) speculated that GX 9+9 has an early type (earlier than G5) companion. Haswell & Abbott (1994) suggested that GX 9+9 is a persistent superhumper, based on its supposed mass ratio ( $q < 0.28$ ), the optical modulations, and the change in the shape of the optical lightcurves. Superhumps are periodic optical modulations first observed in SU UMa dwarf novae (see Warner 1995), but also in black hole soft X-ray transients (O’Donoghue & Charles 1996), and are due to an eccentric accretion disk that is undergoing precession (e.g. Whitehurst 1988).

Recent simultaneous X-ray and optical observations by Kong et al. (2006) did not detect a significant X-ray/optical correlation. Although they could not confirm the X-ray modulation at the orbital period, it is present in the RXTE/ASM data (Levine et al. 2006a,b). Time resolved X-ray spectroscopy by Kong et al. (2006) showed that a two-component spectral model was needed to fit the X-ray emission. The best model suggested that an optically thick boundary layer which is partly obscured (by either the inner disk or thickened disk) and an extended hot corona are present in GX 9+9.

In this paper we present VLT medium resolution blue spectroscopy of GX 9+9, and we derive a new ephemeris based on X-ray data. We determine radial velocity curves and Doppler maps of the most important lines and use these to derive the first constraints on the system parameters.

## 2 OBSERVATIONS AND DATA REDUCTION

On June 24 2003 we obtained two spectra of GX 9+9 in order to establish the strength and velocity structure of its Bowen blend. This was followed by a phase-resolved study from 25 to 27 May 2004 using the FORS 2 spectrograph attached to the VLT Unit 4 (Yepun Telescope) at Paranal Observatory (ESO). During each night in 2004 we observed GX 9+9 for approximately one full orbit with the 1400V volume-phased

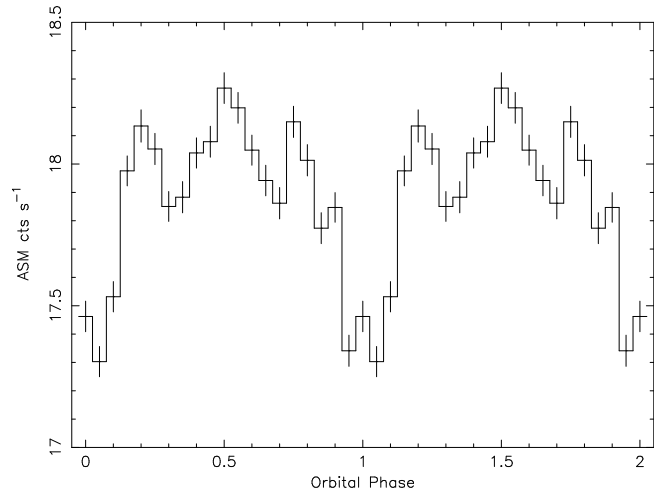


**Figure 2.** Folded RXTE/ASM X-ray lightcurve of GX 9+9 on the orbital period, where phase zero is defined as the minimum in the lightcurve. For clarity, the lightcurve is shown twice.

holographic grism, resulting in a total of 58 spectra (+2 in 2003) with an integration time of 600 s each. We used a slit width of  $0.7''$ , giving a wavelength coverage of  $\lambda\lambda 4514\text{--}5815$  with a resolution of  $70 \text{ km s}^{-1}$  (FWHM). We also observed GX 9+9 once with a wide, 2.0 arcsec slit width. The seeing during these three nights varied between 0.5 and 2.1 arcsec, and was 1.1 arcsec during the observation with the wide slit. The slit was orientated at a position angle of  $-58.5^\circ$  to include a comparison star in order to correct for slit losses. Since we do not have a flux standard, we were not able to correct for the instrumental sensitivity curve. During the daytime He, Ne, Hg and Cd arc lamp exposures were taken for wavelength calibration. We determined the pixel-to-wavelength scale using a 4th order polynomial fit to 20 reference lines giving a dispersion of  $0.64 \text{ \AA pixel}^{-1}$  and rms scatter  $< 0.05 \text{ \AA}$ . We de-biased and flat-fielded all the images and used optimal extraction techniques to maximise the signal-to-noise ratio of the extracted spectra (Horne 1986), using the routines from the PAMELA package. We also corrected for any velocity drifts due to instrumental flexure (always  $< 5 \text{ km s}^{-1}$ ) by cross-correlating with the sky spectra. The subsequent analysis was performed using the package MOLLY.

## 3 DATA ANALYSIS

### 3.1 Orbital period

The first, and only, optical orbital ephemeris of GX 9+9 was published by Schaefer (1990) over 16 years ago. Unfortunately, due to the propagation of the phase uncertainty, this ephemeris cannot be projected to the present. However, Levine et al. (2006a,b) showed that it is possible to detect the orbital period in the publicly available X-ray lightcurve provided by the All Sky Monitor onboard the RXTE satellite (RXTE/ASM). Therefore, we decided to derive a new ephemeris from this dataset by also searching for the 4.2 hrs period and determine a new zero point, using the indi-

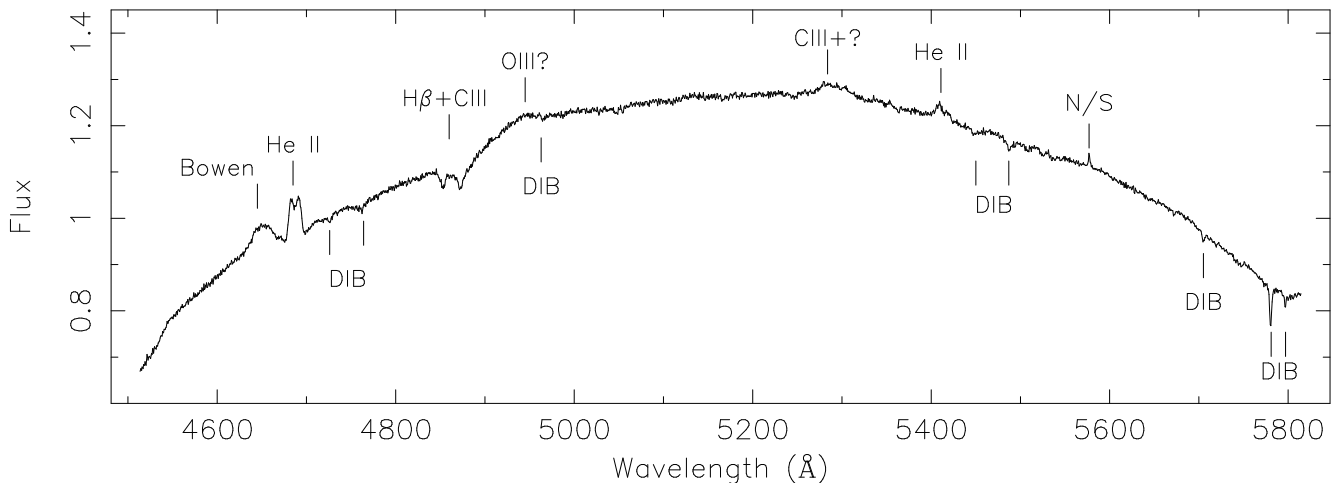


**Figure 3.** Average normalised spectrum of GX 9+9 from our 3 nights of VLT data. We have indicated the most prominent emission lines and interstellar diffuse bands (DIB). Furthermore we have indicated a sky line (N/S) that has not been properly removed.

vidual dwell, full 2-12 keV band-pass observations. We applied a barycentre correction to the data using the IDL routine `HELIO_JD` and searched for the orbital period with the Lomb-Scargle technique (Scargle 1982). Only one significant peak is observed, at 4.19345(2) hrs (see Fig. 1). This value is similar to that of Levine et al. (2006b), but note that this period is slightly, but according to the formal errors significantly ( $4.7\sigma$ ), shorter than the photometric period of  $4.1958 \pm 0.0005$  hrs detected by Kong et al. (2006). In order to see if this difference is due to a change in period, we have also split the RXTE/ASM dataset in two equal lengths and determined the orbital period for each. However, both periods are equal, and we conclude that the orbital period has not significantly changed over the  $\approx 11$  yr baseline of the RXTE/ASM data.

We phase-folded all the data on the observed period and fitted a sine curve, using a date close to our observations as the zero point. We then determined the minimum in our folded RXTE/ASM lightcurve to be JD 2453151.464(3), and define this as orbital phase zero. In Fig. 2 we show the folded lightcurve. Although the lightcurve exhibits a modulation of  $\approx 4\%$ , comparable to that observed by Hertz & Wood (1988), Levine et al. (2006a) reported that the amplitude changes over time and even increased up to 18% after Jan 2005. Note that we define our orbital phase to be half an orbit removed from that used by Schaefer (1990), i.e. more in line with the standard definition where phase zero corresponds to inferior conjunction of the secondary star. This gives a new ephemeris (in HJD) of:

$$T = 2453151.464(3) + 0.1747272(8)E$$

which we will use in the remainder of this paper. In Sects. 3.3 and 3.5 we will determine the ephemeris in three different, independent, ways. They are all consistent with the above ephemeris, giving us confidence that it represents a reliable orbital phasing. However, we must always be careful with the assumption that the minimum in the lightcurve corresponds to inferior conjunction of the secondary star.

### 3.2 Flux calibration and spectrum

In order to correct for slit losses due to the variable seeing we used a comparison star placed on the slit. We divided all comparison star spectra by its wide-slit spectrum, and fitted them with a low-order spline. The spectra of GX 9+9 were subsequently divided by the comparison star splines (corresponding to the same observation) in order to get the final spectra corrected for slit losses. Note that since we do not have a flux standard all our spectra have relative fluxes.

Figure 3 shows the average spectrum of GX 9+9 normalised to unity. It is dominated by high excitation emission lines from He II  $\lambda 4686$ ,  $\lambda 5411$  and Bowen  $\lambda\lambda 4630-4650$ . A strong absorption feature with emission structure superposed is present around  $H\beta$ . Several absorption lines can also be observed that are mainly due to interstellar bands (indicated in Fig. 3 as DIB). A close inspection of the Bowen region shows that there is little emission below 4640 Å, i.e. the part of the blend where all the dominant N III fluorescence lines should be. In order to quantify this absence of N III we measured the centroid of the Bowen region using a Gaussian, and find a central wavelength of  $4648.0 \pm 0.2$  Å (while He II has a central wavelength of  $4686.7 \pm 0.2$  Å). This central wavelength is much higher than was the case for e.g. V801 Ara (4643.2 Å) and V926 Sco (4641.5 Å; Casares et al. 2006). Although there might be some N III present, it does suggest that the Bowen blend is dominated by C III in GX 9+9. We therefore checked where other strong C III transitions should occur in our spectra. There should be one emission line at 4860 Å, with a transition strength comparable to those in the Bowen region. Although this is close to  $H\beta$  we will show in Sect. 3.5 that we have most likely detected it, although the presence of He II  $\lambda 4859$  can also not be ruled out. Another strong C III transition occurs at 5305 Å, and is also present in our spectrum (indicated in Fig. 3), although the width of the line suggests that it is a blend with other unknown lines. Finally, we checked if any strong N III or He I lines are present in our spectral range (apart from the N III lines in the Bowen region). Although there should be 3 strong N III lines at 4867, 5059 and 5320 Å and

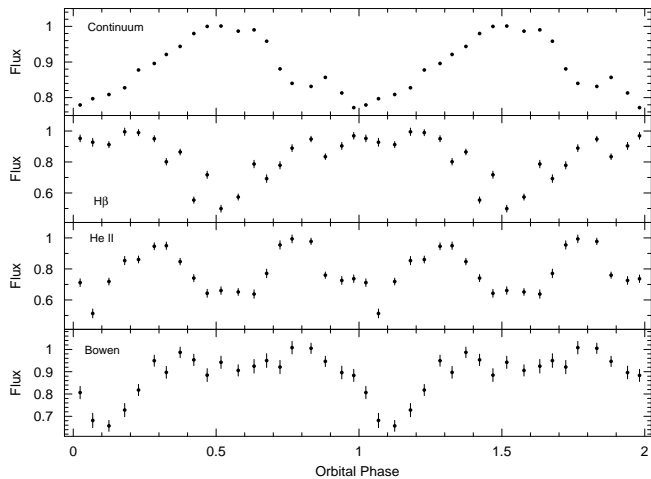


**Figure 4.** Average lightcurves of GX 9+9 with the maximum normalised to unity (also for  $H\beta$ , despite negative flux levels) and folded on the orbital period of 4.19 hrs for the continuum,  $H\beta$ , He II  $\lambda 4686$  and the Bowen blend respectively. For clarity each lightcurve is plotted twice.

2 He I lines at 4922 and 5015 Å, none of these appear to be present.

### 3.3 Optical lightcurves

We used the orbital ephemeris derived above (Sect. 3.1) to compute the orbital phase of each spectrum. We integrated the continuum flux from each individual spectrum, phase-folded them into 20 bins, and normalised the peak flux to unity in order to create the lightcurve that is shown at the top of Fig. 4. The first thing to note is that the minimum in the optical continuum lightcurve corresponds very well with orbital phase 0 as defined by the X-ray modulation, and thereby strengthening our interpretation that the X-ray ephemeris represents inferior conjunction of the secondary. Furthermore, we also note that the flux varies by  $\approx 20\%$ , comparable to previous observations (e.g. Schaefer 1990, Kong et al. 2006).

We have also subtracted the continuum lightcurve from each spectrum in order to derive light curves from the main emission or absorption lines, and these are also shown in Fig. 4. We do note that on average the flux in the lines vary by 40%, i.e. the variation is twice as strong as in the continuum. The flux of the  $H\beta$  absorption line shows more or less a sinusoidal variation, with minimum (i.e. maximum absorption) occurring around orbital phase 0.5 (in anti-phase with the continuum emission). The variation of He II  $\lambda 4686$  and the Bowen blend is more complex. He II  $\lambda 4686$  appears to be a combination of the  $H\beta$  and continuum lightcurves, i.e. showing a minimum around orbital phase 0.5 and a second minimum at phase 1.0. The Bowen emission, on the other hand, looks similar to the continuum emission, although its single minimum is at a slightly later orbital phase of  $\approx 1.1$ .

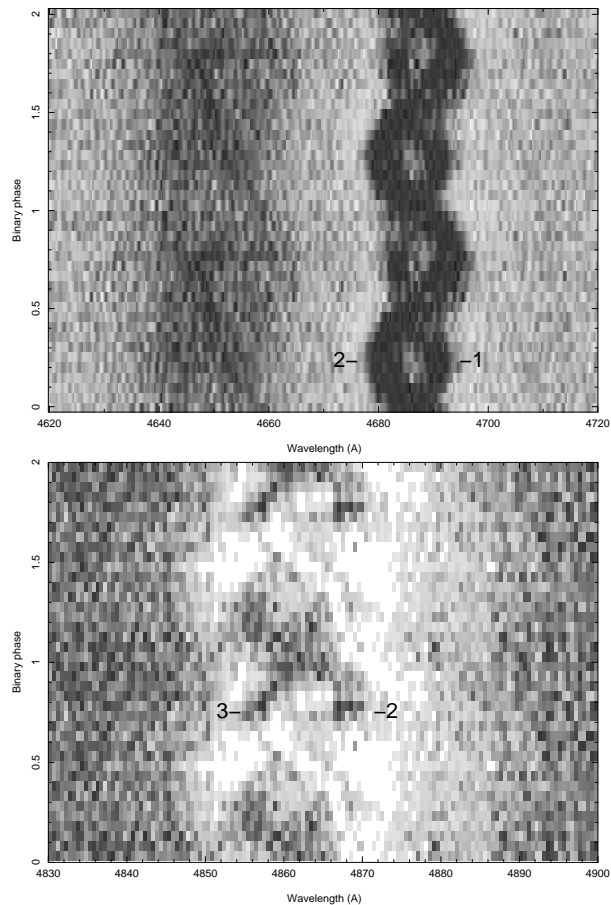


**Figure 5.** Trail of the Bowen blend and He II  $\lambda 4686$  line (top panel), and  $H\beta$  (bottom panel), folded on the orbital period and plotted twice for clarity. The numbers indicated in the trails correspond to the component numbers in Table 1. The light areas in the  $H\beta$  trail are the absorption feature, while dark regions are the emission features.

### 3.4 Trailed spectra and radial velocity curves

We have phase-folded all data into 20 bins, and plotted a trail of the region around He II  $\lambda 4686$  and the Bowen blend in Fig. 5 (top panel). The He II  $\lambda 4686$  line clearly consists of two separate components that we have indicated with 1 and 2 in Fig. 5 and correspond to the component number in Table 1. Both components show a sine-like modulation in anti-phase with each other. Note that these oppositely phased S-waves also produce double peaks, but these are completely different from the more conventional disk dominated line profiles where the peaks move together in phase. There is no strong broad component visible, indicating that most of the He II  $\lambda 4686$  observed is coming from two distinct regions in the binary. We estimated the centre of each emission component as a function of orbital phase using two Gaussians, and then fitted each component with a sine curve, obtaining the parameters given in Table 1. Fig. 5 already suggests that component 2 has twice the velocity amplitude of component 1, and this is confirmed in Table 1.

We also examined the region around  $H\beta$  in more detail, and show a trail in Fig. 5 (bottom panel). Due to the pres-

**Table 1.** Kinematics of GX 9+9 emission line structures obtained by best fitting sine-curves to the double peaked structure observed in He II  $\lambda 4686$  and H $\beta$  regions. The component numbers for He II correspond to the numbers indicated in the He II trail of Fig. 5, and H $\beta$  component 2 has the same origin as component 2 in He II.

	component #	$K$ (km s $^{-1}$ )	$\gamma$ (km s $^{-1}$ )	$\phi$
He II	1	217 $\pm$ 5	97 $\pm$ 5	0.07 $\pm$ 0.05
He II	2	402 $\pm$ 3	91 $\pm$ 3	0.55 $\pm$ 0.05
C III	3	260 $\pm$ 5	87 $\pm$ 5	0.02 $\pm$ 0.05
H $\beta$	2	398 $\pm$ 8	100 $\pm$ 6	0.49 $\pm$ 0.05

$K$ =semi-amplitude,  $\gamma$ = off-set to rest-wavelength,  
 $\phi$ =phase zero

ence of the absorption feature this region is more complex. However, we do notice that the emission feature also appears to consist of two components (indicated with 2 and 3), more or less in anti-phase with each other. These components are clearly visible in the individual spectra (see e.g. Fig. 6), and made us confident that we could again fit two Gaussians to the emission components (see also Table 1 for the best fitting sine curves, which we have labelled C III and H $\beta$ ). We note that the strongest feature (called component 2) appears to originate from the same region as component 2 of He II  $\lambda 4686$ , and we will discuss this in more detail in Sect. 3.5. On the other hand, if we assume that component 3 is also H $\beta$  emission, its average velocity,  $\gamma$ , is completely different compared to all the other components listed in Table 1 ( $\gamma$  would be  $-16$  km s $^{-1}$  compared to  $\approx 95$  km s $^{-1}$ ). However, if we assume this line is C III  $\lambda 4859.65$  and/or He II  $\lambda 4859.3$  (see Sect. 3.2)  $\gamma$  becomes comparable with that derived for the other emission lines. We, therefore, conclude that component 3 is most likely tracing a combination of C III and He II. In Sect. 3.5 we will show that this region is most likely dominated by C III and H $\beta$  emission, and despite its complicated appearance this trail is very similar to He II  $\lambda 4686$ .

In the H $\beta$  trail (Fig. 5) it appears that no net emission components are present at orbital phase 0.5. However, given that the absorption feature hardly moves with orbital phase, we expect the emission feature to be at the deepest point of the absorption feature at orbital phase 0.5. If the peak flux of the emission feature is below the continuum level it would be difficult to detect its signature in the trail. In Fig. 6 we show the average spectrum around orbital phase 0.5, and it is clear that the H $\beta$  and C III/He II emission components are still present (but have peak fluxes below the continuum level).

We also created trails of each individual night by folding them on the ephemeris determined in Sect. 3.1. If GX 9+9 is a superhumper, it would most likely show a similar spectroscopic signature as other superhumping LMXBs, namely a movement in the nightly mean emission line profiles (see e.g. Zurita et al. 2002). Therefore, we did test if movement is present, but no shift in the line centroid was detected between the different nights. Also a comparison between the 2003 and 2004 spectra shows no clear shift that would unambiguously point toward a spectroscopic signature of a superhump in GX 9+9.

In order to determine the radial velocity of the compact

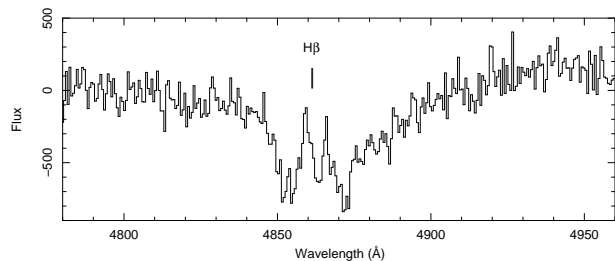


**Figure 6.** Average spectrum of the H $\beta$  region of GX 9+9 around orbital phase 0.5, clearly showing that the main emission components superposed on the broad absorption are still present.

object one can apply the double-Gaussian technique (Schneider & Young 1980). We must note that this technique only works for a standard double peaked emission profile disk, which is clearly not observed in GX 9+9 (see Fig. 5). We still decided to apply the technique to He II  $\lambda 4686$  using velocities that are as far as possible from the prominent emission features in the trail, in the hope that their contribution is negligible. We used a double Gaussian bandpass with FWHM of 100 km s $^{-1}$  and Gaussian separations between 600 and 1200 km s $^{-1}$ . Fig. 7 shows that as we move away from the line core, the  $K_1$  velocity exponentially declines to  $120 \pm 10$  km s $^{-1}$ , while the systemic velocity,  $\gamma$ , moves between 100 and 123 km s $^{-1}$ . The phasing for the compact object showed a small change over Gaussian separation, but corresponds well with the value predicted by the ephemeris derived above (i.e.  $\approx 0.5$ ). Although we expect this kind of behaviour for the  $K_1$  velocity we are still hesitant to identify this as the true motion of the compact object, and we should treat the result with caution.

### 3.5 Doppler maps

Doppler tomography is a powerful tool for probing the structure of the accretion disk (Marsh & Horne 1988). It makes use of all the available data and is effective for emission features that are too weak to be identified in the individual spectra, by resolving the distribution of the line emission in the co-rotating frame of the binary system. The definition of orbital phase 0 in Doppler maps corresponds to inferior conjunction of the secondary (Marsh 2001), and is one of the main reasons why we changed the definition of our phase 0 compared to that adopted by Schaefer (1990). This should project a signature of the donor star along the positive y-axis (Steehgs & Casares 2002).

Fig. 8 shows the Doppler maps of the three most important emission line regions, i.e. He II  $\lambda 4686$ , the Bowen blend and H $\beta$ . Since there are no other emission lines present around He II, we could use the standard reduction techniques with a systemic velocity of 90 km s $^{-1}$ . As expected from the trails (see Sect. 3.4) two main emission regions can be observed (Fig. 8/top-left), more or less in anti-phase with each other. The bright region in the top half corresponds with the position where the donor star and accretion stream are expected to be located. However, the brightest feature is the extended region in the bottom-left quadrant of the

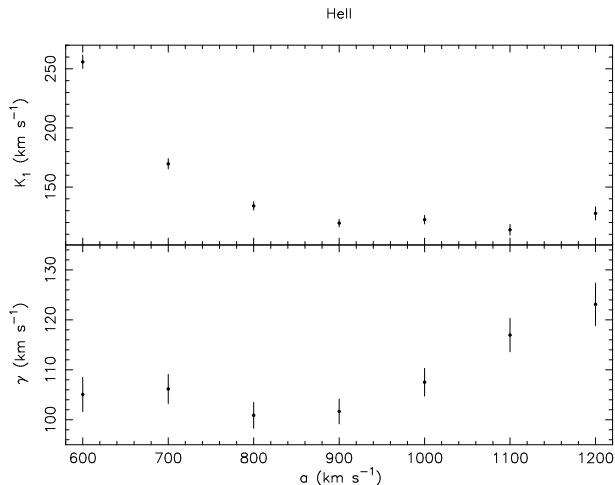


**Figure 7.** Diagnostic diagram for GX 9+9 of He II  $\lambda 4686$  to follow the estimates of the radial velocity of the compact object,  $K_1$ , and the systemic velocity,  $\gamma$ , as a function of Gaussian separation,  $a$ .

Doppler map, a position where no enhanced emission is expected for a 'normal' X-ray binary.

Using the correct systemic velocity should produce the sharpest defined feature in the top part of the Doppler map. We therefore tried different velocities with steps of  $10 \text{ km s}^{-1}$  around  $90 \text{ km s}^{-1}$ . However, in line with Sect. 3.4, we found that  $90 \text{ km s}^{-1}$  gives the sharpest result for the compact spot in the top part of the map, and again interpreted this as the systemic velocity. Furthermore, we created Doppler maps of He II  $\lambda 4686$  for each individual night in order to explore any significant change. All maps looked identical, and no long-term change in the emission line profile appears to be present.

The Doppler map of the Bowen region (Fig. 8/top-right) was created using standard reduction techniques, but fitting the three strongest C III lines ( $4647, 4650$  and  $4665 \text{ \AA}$ ) simultaneously using relative strengths as indicated by McClintock et al. (1975). The most pronounced feature in the map is a sharp spot in the top half of the map, at a position similar to that in the He II map and where the donor star is expected. Fitting a 2-dimensional Gaussian to this spot we measure a velocity of  $250 \pm 25 \text{ km s}^{-1}$ . This  $25 \text{ km s}^{-1}$  is the formal 1-sigma fitting error in the centroid position of our 2-dimensional Gaussian. Although the spot is offset from the x-axis by  $35 \text{ km s}^{-1}$ , this only corresponds to a phase offset of 0.02 which is smaller than the error in the phase origin (0.04). The spot location is thus consistent with being along the axis connecting the neutron star with the donor star. We also rotated the map by 0.02 orbital phase in order to align the spot with the x-axis. Since we measured a similar velocity as above, we concluded that the error introduced by the off-set is negligible.

The most complex region is H $\beta$ , where C III  $\lambda 4860$ /He II  $\lambda 4859$  and an H $\beta$  emission line are superposed on a deep absorption feature. Since it is currently not possible to directly create Doppler maps with negative pixel values we used a non-standard reduction technique. First we created a Doppler image that consisted of a Gaussian with a peak and width comparable to the observed absorption feature.

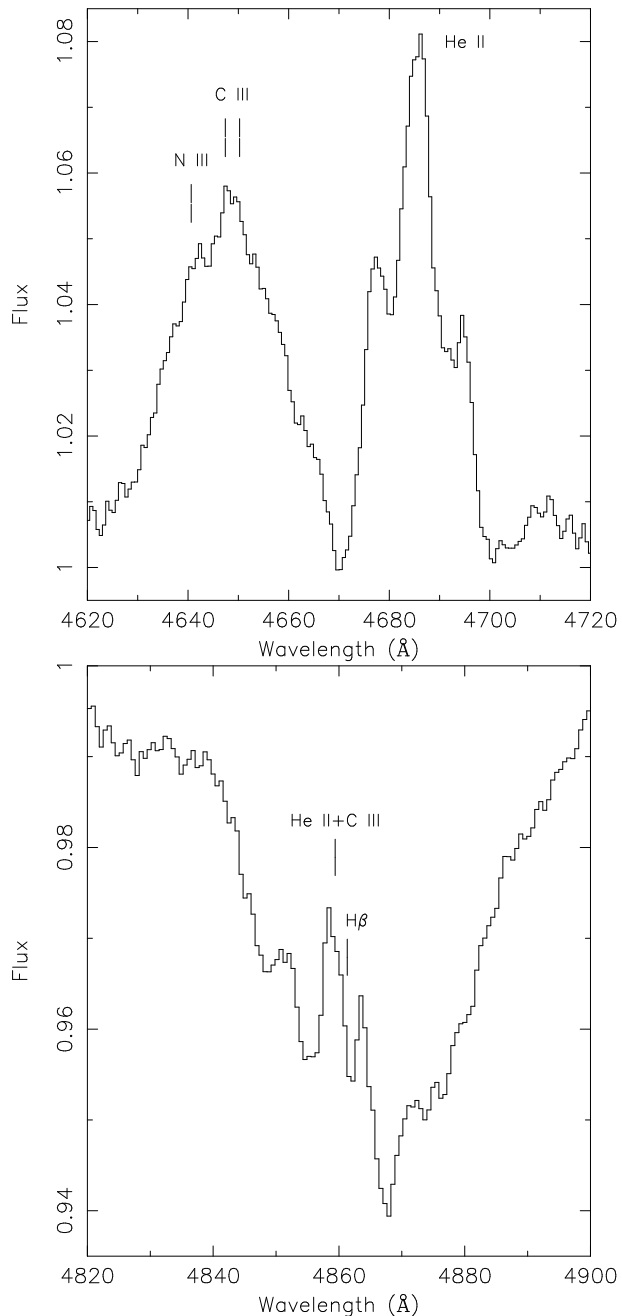


**Figure 9.** Average spectrum of the Bowen (top) and H $\beta$  (bottom) regions of GX 9+9 in the rest-frame of the donor star. We have indicated the dominant contributing lines in these regions.

From this image we created artificial data that has the same properties as the observations, i.e. creating a trail of Gaussians. We then added the artificial data to the observations in order to remove the absorption feature. We then used standard analysis techniques to create Doppler images for both the C III/He II and H $\beta$  simultaneously. Finally, we subtracted the artificial map of the Gaussian to produce the maps shown in Fig. 8 (bottom). Although we were able to more or less disentangle the different components, we must be cautious about the details of the two maps.

The C III/He II Doppler map (Fig. 8/bottom-right)

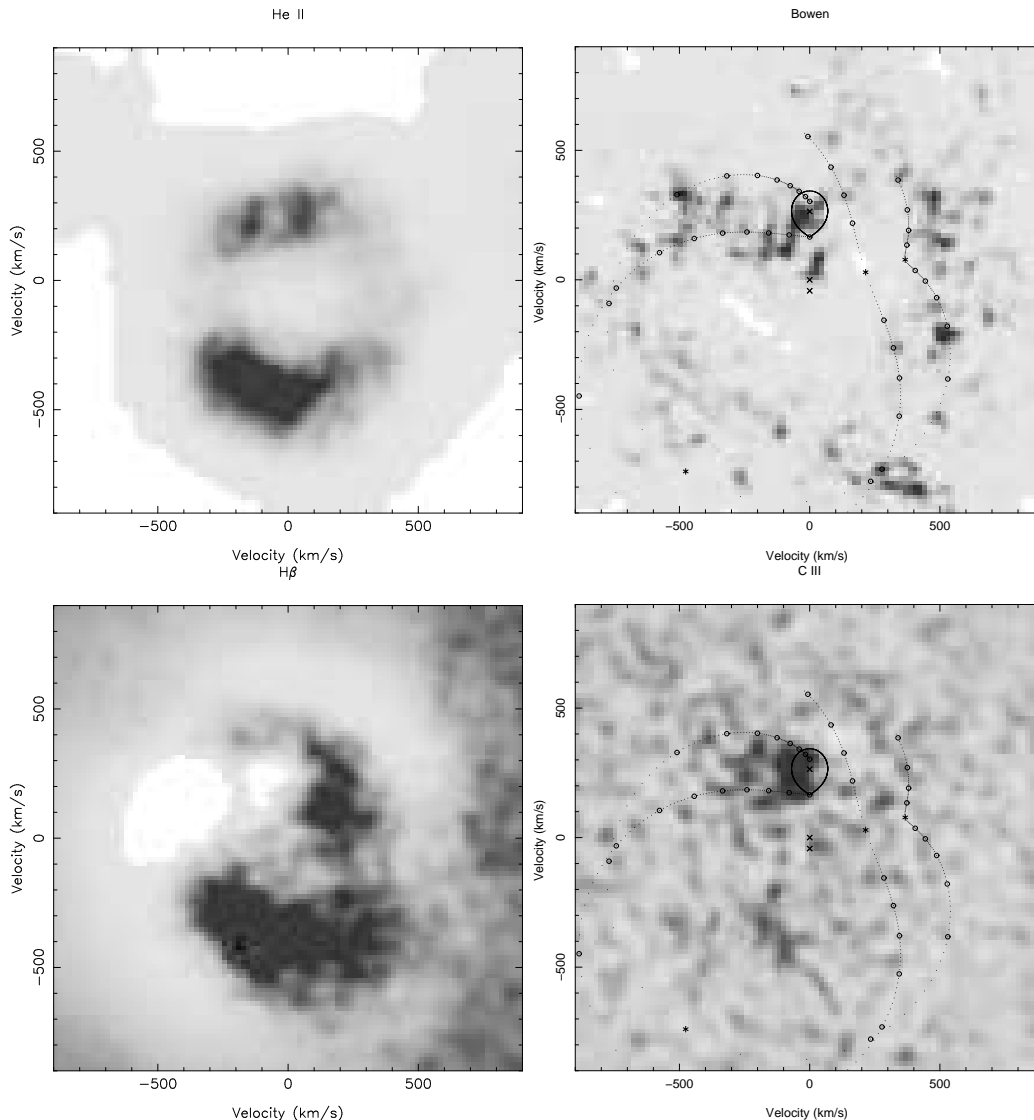


**Figure 8.** Doppler maps of He II  $\lambda 4686$  (top-left), the Bowen region (top-right). The bottom panel shows the Doppler deconvolution of the H $\beta$  (bottom-left) and C III  $\lambda 4860$  components as explained in Sect. 3.5. In He II, Bowen and C III the white parts indicate the zero level of the flux, while in H $\beta$  the white parts indicate regions of most absorption. Indicated on the Bowen and C III maps are the Roche lobe, gas stream leaving the L1 point, and the Keplerian velocity along the stream for the set of parameters  $q=0.16$  and  $K_2=264$  km s $^{-1}$  discussed in Sect. 4.2.

looks remarkably similar to that of the Bowen region, suggesting that the line is indeed dominated by C III emission. The main feature is a single localised spot in the top half of the map, that is at a velocity of  $210 \pm 25$  km s $^{-1}$  (and an off-set from the x-axis of  $\approx 55$  km s $^{-1}$ , still within our phase zero uncertainty), consistent with the spot in the Bowen map. The H $\beta$  map (Fig. 8/bottom-left) looks more complex. All absorption is attributed to H $\beta$  and is present at all orbital phases, although it is most prominent in the left part of the map around  $y=0$ ,  $x=-500$  km s $^{-1}$ . Note that in this map the lightest regions indicate negative flux levels, in sharp contrast with the other maps where lightest regions represent the continuum level. However, the most prominent feature in the H $\beta$  map is created by the emission lines, namely the extended region in the bottom half of the map that has a comparable shape and position to that in

the He II map. However, this similarity between the H $\beta$  and He II maps is rather curious, since in other LMXBs these lines can show rather different characteristics (e.g. Steeghs & Casares 2002). Although this might be explained by contamination of He II  $\lambda 4859$ , we would have expected that this would mainly affect the C III map. We must, therefore, conclude that this emission region in the bottom half of the H $\beta$  map is likely real.

#### 4 DISCUSSION

We have presented medium resolution optical spectroscopy of GX 9+9. One of the most remarkable characteristics of GX 9+9 is the strong C III emission in its spectrum, while N III is hardly detected. To our knowledge, no other X-ray binary is known that shows such an unusual C III/N III ra-

**Table 2.** Derived system parameters for GX 9+9.

Parameter	Parameter	Parameter	Parameter
$P_{\text{orb}}$ (hrs)	4.1934528(20)	$f(M)$ ( $M_{\odot}$ )	( $\geq$ )0.22 $\pm$ 0.03
$T_0$ (HJD)	2 453 151.464(3)	$q$ ( $M_2/M_1$ )	0.07-0.35
$\gamma$ ( $\text{km s}^{-1}$ )	90 $\pm$ 7	$K_2$ ( $\text{km s}^{-1}$ )	182-406
$K_{\text{em}}$ ( $\text{km s}^{-1}$ )	230 $\pm$ 35		

tio in the Bowen region. For example, in X1822–371 and Sco X-1 the narrow Carbon and Nitrogen lines in the Bowen region were more or less of comparable strength, and no other strong C III/N III lines could be detected (Casares et al. 2003, Steeghs & Casares 2002). This could give us important constraints on the evolutionary status of GX 9+9. However, we can exclude a more evolved core in the donor star of GX 9+9, since this would lead to an overabundance of N III due to processing by the CNO cycle as has been observed in e.g. XTE J1118+480 Haswell et al. (2002). The only other systems that show prominent Carbon emission lines in their spectra are some of the ultra-compact X-ray binaries (Nelemans et al. 2006). However, in these systems the donor star is thought to be a white dwarf that is deficient of both H and He. These systems are clearly different to GX 9+9, which is not an ultra-compact X-ray binary and has both H and He in its spectrum.

#### 4.1 Orbital Period and Long Term Variations

Following Levine et al. (2006a,b) we have updated the ephemeris of GX 9+9 using the RXTE/ASM data. Given the coincidence of optical minimum with the minimum in the X-ray lightcurve, as well as the presence of Bowen emission spots on the y-axis consistent with the donor star, we feel confident that this ephemeris tracks the correct orbital phase of the binary. Levine et al. (2006a) showed that the strength of the modulation in GX 9+9 increased from 6% before Jan 2005 to 18% after this date (and until at least June 2006). A possible explanation for this change in modulation is given by the folded RXTE/ASM lightcurve shown in Fig. 2. There appears to be a partial eclipse around orbital phase 0, i.e. at inferior conjunction of the secondary. The most likely region that could be eclipsed by the secondary is the extended accretion disk corona that Kong et al. (2006) observed in GX 9+9, suggesting that the corona slowly changes size. One option could be that the orbital modulation in X-rays disappears when the corona becomes too small to be eclipsed by the secondary. An alternative option is that the corona is always eclipsed, but when it increases in size its fractional contribution to the total X-ray flux increases thereby lowering the depth of the eclipse. If the size of this corona could be determined, we would be able to distinguish between the different scenarios, and could also constrain the inclination of GX 9+9. However, the fact that this partial eclipse occurs suggests a reasonably high inclination.

Haswell et al. (2001) proposed that GX 9+9 is a persistent superhumper. Superhumps are periodic optical modulations first observed during outburst of SU UMa dwarf novae (see Warner 1995 for a review), and their most important property is that the photometric period is a few percent (1-

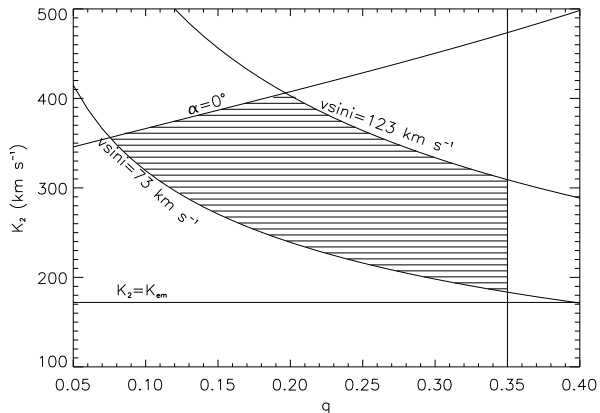


**Figure 10.** Constraints on  $q$  and  $K_2$  for GX 9+9.  $K_2$  must be larger than  $K_{\text{em}}$ , and a disc opening angle of  $\alpha=0$  gives the upper-limit for  $K_2$ . The rotational broadening derived from the emission line widths sets a lower limit to  $q$ , while the largest possible main sequence star that fits the Roche-lobe of GX 9+9, combined with its maximum allowed broadening sets the upper-limit to  $q$ . All curves indicate 95% confidence levels.

7%) longer than the orbital period. This is thought to be due to prograde precession of an eccentric accretion disk, giving rise to slightly longer periods (with respect to the orbital period) for the accretion disk. The main criterion for creating an eccentric disk is an extreme mass ratio ( $M_2/M_1 < 0.33$ ). Comparing our X-ray period with the photometric period derived by Kong et al. (2006) we note that the photometric one is 0.0564 hrs longer, corresponding to only  $\simeq 1\%$  of the orbital period. Although this difference is small, it is still significant according to the formal errors ( $4.7\sigma$ ), and we therefore further investigated the possibility of a superhump in GX 9+9.

If GX 9+9 is a superhumper, we would also expect similar spectroscopic characteristics for GX 9+9 to that of the known superhumping LMXB XTE J1118+480, namely the movement of the nightly mean emission line profiles (e.g. Zurita et al. 2002). Such movement is not observed in GX 9+9, arguing against a superhump interpretation. Furthermore, also the so-called  $\epsilon(q)$ - $q$  relation, where  $q$  is the mass ratio and  $\epsilon(q)$  the fractional period excess of the superhump over the orbital period, suggest that the photometric period cannot be due to a superhump. If the difference in photometric and X-ray period is real, the empirical relation by Patterson et al. (2005) suggests that  $q \simeq 0.003$ , an unrealistically small value (as we will show in Sect. 4.2). This could indicate that the errors on the orbital periods have been underestimated, and that the X-ray and photometric period are similar. On the other hand we cannot completely exclude the possibility that the movement of the nightly mean emission line profile is hidden by the strong emission feature in the lower-left quadrant of the Doppler maps (Fig. 8), and that the  $\epsilon(q)$ - $q$  does not apply to persistently bright LMXBs. The only thing we therefore conclude is that there are no indications of a superhump in our dataset, and that a better determination of the photometric period is needed to find out if the difference with the X-ray period is real.



## 4.2 Donor Star and System Parameters of GX 9+9

Thus far narrow lines in the Bowen region have been detected in Sco X-1, X 1822–371, GX 339–4, 4U 1636–53, 4U 1735–44 and Aql X-1 (Steeeghs & Casares 2002; Casares et al. 2003, Hynes et al. 2003, Casares et al. 2006, Cornelisse et al. 2007). We can now also add GX 9+9 to this list. Phase zero of the radial velocity curve of these narrow lines in GX 9+9 correspond well with the minima in the X-ray and optical lightcurves, suggesting that these lines arise close to or are connected with the donor star. It has been proposed for the other sources that these narrow lines arise on the surface of the secondary, and especially for the eclipsing LMXB X 1822–371 this connection could unambiguously be claimed (Casares. 2003). Since it is possible, for a valid set of system parameters (see below), to draw a Roche lobe on the Bowen and C III Doppler maps that encompasses most of the observed narrow spots (see Fig. 8), we propose that also in the case of GX 9+9 these lines arise on the donor star. If our suggestion is correct, the narrow feature in the Doppler maps of both the Bowen region and C III  $\lambda 4860$  (see Fig. 8) must be produced somewhere on the inner hemisphere of the companion, and has a  $K_{\text{em}}$  of  $230 \pm 35 \text{ km s}^{-1}$  (the average value derived from the compact spots in the Doppler maps of He II  $\lambda 4686$ , Bowen and C III  $\lambda 4860$ ). However, given that only the irradiated side facing the compact object is contributing to this emission, this should be considered a lower-limit to the velocity semi-amplitude of the centre of mass of the donor  $K_2$ .

In order to derive some constraints on the system parameters of GX 9+9, we can start by determining a lower limit on the mass function of  $f(M) = M_1 \sin^3 i / (1 + q)^2 > 0.22 \pm 0.03 M_\odot$  (where  $q = M_2/M_1$  is the mass ratio and  $i$  the inclination of GX 9+9). This lower limit corresponds with the assumption that  $K_{\text{em}} = K_2$ , i.e. that the narrow lines are produced on the poles of the donor star. In order to find the real  $K_2$  we need to determine the  $K$ -correction, which is dependent on the disk flaring angle ( $\alpha$ ),  $q$ , and weakly on  $i$  (see Muñoz-Darias et al. 2005). Using an irradiation binary code, Muñoz-Darias et al. determined 4th order polynomials for different values of  $\alpha$  and  $i$  to estimate the  $K$ -correction. Unfortunately we do not have any solid estimates of  $K_1$ , since the double Gaussian method used in Sect. 3.4 is not valid for an accretion disk that is dominated by a hotspot. Therefore we cannot directly apply the  $K$ -correction, and must therefore resort to several assumption in order to further constrain the system parameters. Although we will point out what the major source of uncertainty is for each of our assumptions, we do think that they are currently the best we can do.

First of all, the simplest assumption is that  $K_2 \geq K_{\text{em}}$ , and show the 95% confidence limit in Fig. 10. Furthermore, we can use the polynomials by Muñoz-Darias et al. (2005) for  $\alpha = 0^\circ$  (and  $i = 40^\circ$ ) to determine the upper-limit to  $K_2$  as a function of  $q$ . Again we show the 95% confidence curve in Fig. 10.

We can determine a lower-limit to  $q$  by estimating a lower limit to the rotational broadening,  $V \sin i$ , of the emission lines produced on the surface of the donor (Wade & Horne 1988). However, this does mean that we assume that all of the line broadening is due to rotation, which

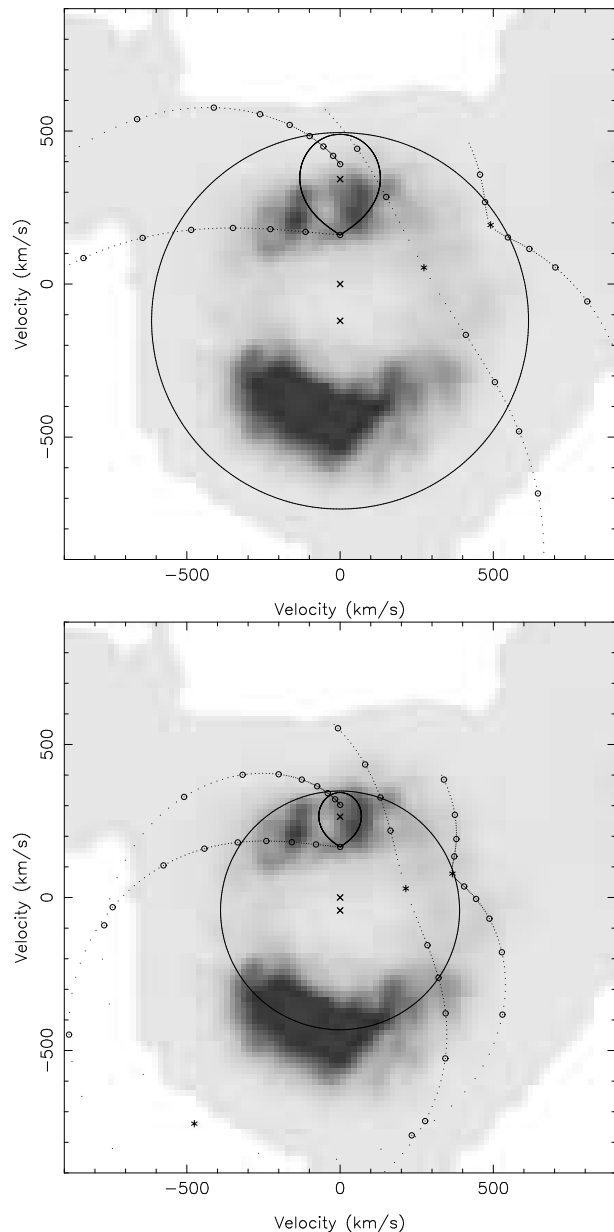


**Figure 11.** He II  $\lambda 4686$  Doppler map showing the Roche lobe of the secondary, the gas stream leaving the L1 point, and the Keplerian velocity along the stream for two different sets of system parameters. The circle indicates the Keplerian velocity at the edge of the disk. Top: System parameters derived for the assumption that  $K_1$  derived with the double Gaussian technique is correct. Bottom: System parameters derived using the assumption that the emission feature in the bottom left quadrant is part of the accretion disk.

might not be the case. We created an average spectrum in the rest-frame of the secondary. Fig. 9 shows the two most prominent regions (around He II  $\lambda 4686$  and H $\beta$ ) of the rest-frame spectrum. Unfortunately, most lines are either too weak, are located in very complicated regions (e.g. Bowen and H $\beta$  regions) or have a component that does not originate on the secondary (e.g. He II  $\lambda 4686$ ). We decided to estimate the  $FWHM$  of the two C III lines in the Bowen

region, C III  $\lambda 4859$ , and also the  $H\beta$  absorption line. All lines give a similar *FWHM* that is on average  $153 \pm 26$  km  $s^{-1}$ . However, we do note that this includes the effect of the intrinsic broadening due to the instrumental resolution of 70 km  $s^{-1}$ . To take this into account we broadened a strong line in our arc spectrum using a Gray rotational profile (Gray 1992) until we reached the observed *FWHM*. We assumed no limb-darkening since the fluorescence lines occur in optically thin conditions. We found that a rotational broadening of  $102 \pm 15$  km  $s^{-1}$  reproduces our results. Using  $V_{\text{rot}} \sin i = 0.462 K_2 q^{1/3} (1+q)^{2/3}$  (Wade & Horne 1988), and  $V \sin i \geq 73$  km  $s^{-1}$  (95% confidence) we can draw this curve in Fig. 10.

We also show the limit corresponding to the assumption that the donor star is a zero-age main sequence star that fits in a 4.2 hrs period Roche lobe. Although there is no guarantee that the donor star in GX 9+9 satisfies that assumption (see e.g. Schenker & King 2002 for alternative scenarios), we include it in Fig. 10 as a likely constraint on the system parameters (Casares et al. 2006). This leads to a donor star mass  $\leq 0.47 M_{\odot}$  and together with  $M_{\text{NS}} \geq 1.35 M_{\odot}$  gives  $q \leq 0.35$ . Note that this implies that the lower limit on  $K_2$  derived from the compact spot in the Bowen and C III Doppler maps is always below the rotational broadening curve determined from the widths of the emission lines.

By estimating the upper-limit to the rotational broadening for a  $0.47 M_{\odot}$  main sequence star donor we derive the final limit shown in Fig. 10. From Paczynski (1974, 1983) we can determine an upper-limit to the inclination of  $\leq 65^{\circ}$ , i.e. where the donor star would just eclipse the compact object. Since Kong et al. (2006) did not detect any orbital variation in X-rays, and their X-ray spectral modelling showed that the emission coming from the inner accretion disk or boundary layer is a significant fraction of the total flux ( $\approx 25\%$ ), we think our assumption on the inclination is valid. This gives a maximum rotational broadening of  $V \sin i = 123$  km  $s^{-1}$ , as indicated in Fig. 10.

The values for the system parameters of GX 9+9 we have derived are the best limits possible, and these are shown in Fig. 10 and tabulated in Table 2. In the remainder of this section we will speculate in two different ways about further constraints on the system parameters using more uncertain assumptions. Although they lead to very different system parameters, we will use the results of these speculations for our discussion of the accretion disk structure in Sect. 4.3.

Although the double Gaussian technique is not an appropriate way to determine  $K_1$  in the case of GX 9+9, the value derived is within the acceptable limits. We can therefore speculate that this is the correct  $K_1$  and see how this limits the system parameters. Again using the polynomials by Muñoz-Darias (2006) we can determine the largest  $K$ -correction, which leads to  $K_2 \leq 369$  km  $s^{-1}$  and thereby  $q \geq 0.32$ . Since we already established that  $q$  must be smaller than 0.35 (see Fig. 10), we derive a lower limit to  $K_2$  of 343 km  $s^{-1}$  in this case. We note that these system parameters are all toward the upper-limits of the allowed area in Fig. 10. We use the lower limits of our derived parameters ( $q=0.35$  and  $K_2=343$  km  $s^{-1}$ ) to draw the Roche-lobe of the secondary, stream trajectories and outer edge of the accretion disk on the Doppler map of He II and show this in Fig. 11 (top panel). We have indicated the Roche lobe of the secondary and the outer edge of the accretion disk as solid lines.

The crosses indicate the velocities of the centre of mass, and the two stars, while the dotted lines indicate the ballistic trajectory of the material leaving the L1 point and the Keplerian velocity the ballistic stream passes through. It is clear from this figure that in this case the emission feature in the lower-left quadrant is at too low velocities to be associated with the accretion disk.

Another way to estimate the system parameters is if we speculate that the emission feature in the lower-left quadrant must be part of the accretion disk. Furthermore, we can also assume that the feature close to the donor star signature is part of the accretion stream. These constraints imply a small  $K_2$  (to make the velocities of the outer edge of the disk similar to the feature in the lower-left) and also a small  $q$  (the Roche-lobe of the secondary must be small to also let the stream pass through the feature close to the donor star). Assuming that our estimate of  $V \sin i$  is correct, there is a possible combination of  $q$  and  $K_2$  at the lower limits of our allowed region ( $q=0.16$  and  $K_2=264$  km  $s^{-1}$  for  $\alpha=12^{\circ}$  and  $i=40^{\circ}$ ) that fulfils all our criteria. and we show the result in Fig. 11 (bottom).

Note that we do not claim that either of the two sets of system parameters shown in Fig. 11 must be correct. Given the large area of possible solutions in Fig. 10 it would be very unlikely that they are, but they nicely illustrate that using different assumptions, both not too unreasonable, it is possible to derive completely different system parameters. In order to really constrain the system parameters of GX 9+9, it is necessary to unambiguously determine  $K_1$ , as was for example possible for X 1822–371 or V801 Ara (Jonker & van der Klis 2001; Casares et al. 2006). Unfortunately, this is going to be difficult for GX 9+9, since thus far it has not been possible to directly observe a signal coming from the compact object (in the form of pulsations or Type I X-ray bursts) or even the most inner regions of the accretion disk (in the form of high frequency quasi-periodic oscillations (e.g. van der Klis 2006)).

### 4.3 Accretion Disk Structure

GX 9+9 shows several interesting characteristics that are not commonly observed in LMXBs. Most important of all is the presence of a strong emission feature in the lower-left quadrant of both the He II  $\lambda 4686$  and  $H\beta$  Doppler maps (see Fig. 8), while another uncommon feature is the extremely broad absorption feature around  $H\beta$  that is present at all phases.

In many LMXBs, the He II Doppler map displays a classic disk-like structure, with sometimes a spot in the upper-left quadrant due to the accretion stream impacting the disk. However, having emission predominantly in the lower-left quadrant of the Doppler map is not unique for GX 9+9. There are at least two LMXBs that show a similar He II Doppler map, the transient sources XTE J2123–058S (Hynes et al. 2001) and GRO J0422+32 (Casares et al. 1995). In particular, a comparison between the He II  $\lambda 4686$  trails of GX 9+9 and XTE J2123–058 shows that they are strikingly similar to each other. Hynes et al. (2001) compared the properties of XTE J2123–058 with that of the SW Sex objects, a subclass of nova-like cataclysmic variables (see e.g. Thorstensen et al 1991). Although there are several competing models, it is generally thought that SW Sex ob-

jects have some sort of stream (that is not connected to the accretion disk), that is either overflowing the disk or being propelled away, that gives rise to their peculiar characteristics (see e.g. Hoard et al. 2003, Hellier 2000, Horne 1999).

In Fig. 11 we show various system characteristics superposed on the He II Doppler map for two different sets of system parameters. The important thing to notice in Fig. 11 (bottom) is that there are combinations of valid system parameters possible where the emission feature in the lower-left quadrant overlaps with the expected velocities for the outer edge of the accretion (although some emission it is still at sub-Keplerian velocities). This suggests that most of the He II emission is produced by material that is carried downstream after the stream impacts the accretion disk. Such behaviour was also observed in EXO 0748–676 where especially emission from the higher ionization emission lines showed up further downstream (Pearson et al. 2006), at a position comparable to the He II emission in GX 9+9. However, there are also many combinations of the system parameters possible where all He II emission in GX 9+9 is at sub-Keplerian velocities (as illustrated in Fig. 11), and that disk overflow must take place. In this case it would be very similar to XTE J2123–058, and it would then be the second LMXB to show SW Sex behaviour (Hynes et al. 2001). Unfortunately, currently we cannot distinguish between both scenarios, and must conclude that both are just as likely.

The presence of the broad absorption component around  $H\beta$  in GX 9+9 is another curious feature. Although other LMXBs also show such a feature, e.g. X 1822–371, Ser X-1 and XTE J2123–058 amongst others (Casares et al. 2003, Hynes et al. 2004, Hynes et al. 2001), it is usually not as strong as observed in GX 9+9. An exception is the X-ray transient GRO J0422+32 (that showed a similar He II  $\lambda 4686$  Doppler map as GX 9+9) where the absorption feature around  $H\beta$  (and  $H\gamma$ ) shows a similar strength (Casares et al. 1995). Although this might be a coincidence, since XTE J2123–058 does not show such prominent absorption (Hynes et al. 2001), it is curious. An explanation could be a high inclination for GX 9+9 that causes absorption by the optically thick parts of the inner accretion disk. This is supported by the shape of the folded X-ray lightcurve (Fig. 2) and the fact that Kong et al. (2006) concluded that a significant fraction of the inner accretion disk or boundary layer is not visible due to obscuration by the inner or thickened disk. Interestingly, XTE J2123–058 and many SW Sex objects also have a high inclination (Casares et al. 1998, Knigge et al. 2000). Although a high inclination has also been suggested for GRO J0422+32 (Kato et al. 1995), there are indications that it is lower (e.g. Gelino & Harrison. 2003; Reynolds et al. 2007).

## 5 CONCLUSIONS

We have presented a spectroscopic dataset of GX 9+9, and using the Bowen fluorescence technique have for the first time detected narrow lines that we interpret as coming from the donor star. If true, this allowed us to determine a lower limit on the mass function of the system of  $0.22M_{\odot}$  and  $182 \leq K_2 \leq 406 \text{ km s}^{-1}$ . In order to constrain the system parameters more information is necessary, in particular on  $K_1$ . However, given that thus far no unambiguous detection of

the compact object has been made this is going to be difficult.

We have updated the ephemeris of GX 9+9 using RXTE/ASM X-ray data, and the folded lightcurve suggests a partial eclipse of the extended accretion disk corona by the secondary. The Doppler maps of GX 9+9 show the presence of stream overflow. This is either of material that is carried downward along the rim of the accretion disk, or overflowing material that is at sub-Keplerian velocities comparable to XTE J2123–058 and SW Sex systems (Hynes et al. 2001). Finally, GX 9+9 shows a curious C III/N III ratio compared to other LMXBs, which could provide an important hint about the evolutionary status of this system.

## ACKNOWLEDGEMENTS

Based on data collected at the European Southern Observatory Paranal, Chile (Obs.Id. 073.D-0819(A)). We would like to thank the referee, Peter Jonker, for the careful and helpful comments which have improved this paper. We would like to thank the RXTE/ASM teams at MIT and GSFC for provision of the on-line ASM data. We acknowledge the use of PAMELA, MOLLY and DOPPLER developed by T.R. Marsh. We acknowledge the use of the on-line atomic line list at <http://www.pa.uky.edu/~peter/atomic>. RC acknowledges financial support from a European Union Marie Curie Intra-European Fellowship (MEIF-CT.2005-024685). JC acknowledges support from the Spanish Ministry of Science and Technology through project AYA2002-03570. DS acknowledges a Smithsonian Astrophysical Observatory Clay fellowship as well as support from NASA through its guest Observer program. DS acknowledges a PPARC/STFC Advanced Fellowship.

## REFERENCES

- Casares J., Martin A.C., Charles P.A., Martin E.L., Reboloto R., Harlaftis E.T., & Castro-Tirado A.J. 1995, MNRAS, 276, L35
- Casares, J., Serra-Ricart, M., Zurita, C., Gomez, A., Alcalde, D., Charles, P. 1998, IAU Circ., 6971
- Casares J., Steeghs D., Hynes R.I, Charles P.A., O'Brien K., 2003, ApJ, 590, 1041
- Casares, J., Cornelisse, R., Steeghs, D., Charles, P.A., Hynes, R.I., O'Brien, K.O., & Strohmayer, T.E. 2006, MNRAS, 373, 1235
- Charles P.A., & Coe M.J. 2006, in “Compact Stellar X-ray Sources”, eds. W.H.G. Lewin and M. van der Klis, CUP, 215
- Cornelisse, R., Casares, J., Steeghs, D., Barnes, A.D., Charles, P.A., Hynes, R.I., & O'Brien, K., 2007, MNRAS, 375, 1463
- Davidson A., Malina R., Bowyer S., 1976, ApJ, 203, 448
- Gelino, D.M., Harrison, T.E. 2003, ApJ, 599, 1254
- Gray, D.F., 1992, “The Observation and Analysis of Stellar Photospheres”, CUP, 20
- Hasinger, G., & van der Klis, M. 1989, A&A, 225, 79
- Haswell, C.A., Abbott, T.M.C. 1994, in “The evolution of X-ray binaries”, eds. Steve Holt and Charles S. Day, AIP, Vol. 308, p.201

- Haswell, C.A., King, A.R., Murray, J.R., & Charles, P.A. 2001, MNRAS, 321, 475
- Haswell, C.A., Hynes, R.I., King, A.R., Schenker, K. 2002, MNRAS, 332, 928
- Hellier, C. 2000, New Ast. Rev., 44, 131
- Hertz P., Wood K.S., 1987, ApJ, 331, 764
- Hoard D.W., Szkody P., Froning C.S., Long K.S., Knigge C. 2003, AJ, 126, 2473
- Horne K., 1986, PASP, 98, 609
- Horne, K. 1999, in ASP Conf. Ser. 157, Annapolis Workshop on Magnetic Cataclysmic Variables, ed. C. Hellier & K. Mukai (San Francisco: ASP), 349
- Hynes R.I., Charles P.A., Haswell C.A., Casares J., Zurita C., & Serra-Ricart M. 2001, MNRAS, 324, 180
- Hynes R.I., Steeghs D., Casares J., Charles P.A., O'Brien K., 2003, ApJ, 583, L95
- Hynes, R.I., Charles, P.A., van Zyl, L., Barnes, A., Steeghs, D. O'Brien, K., Casares, J. 2004, MNRAS, 348, 100
- Jonker, P.G., van der Klis, M. 2001, ApJ, 553, L43
- Kato, T., Mineshige, S., Hirata, R. 1995, PASJ, 47, 31
- van der Klis, M. 2006, in "Compact stellar X-ray sources", eds. W.H.G. Lewin & M. van der Klis, CUP, p. 39
- Knigge, C. Long, K.S., Hoard, D.W., Szkody, P., Dhillon, V.S. 2000, ApJ, 539, L49
- Kong, A.K.H., Charles, P.A., Homer, L., Kuulkers, E., & O'Donoghue, D. 2006, MNRAS, 368, 781
- Levine, A.M., Harris, R.J., & Vilhu, O. 2006a, ATEL, 839
- Levine, A.M., & Corbet, R. 2006b, ATEL, 940
- Marsh T.R., 2001, in Astrotomography, Indirect Imaging Methods in Observational Astronomy, eds. H.M.J. Boffin, D. Steeghs and J. Cuypers (Lecture Notes in Physics) vol. 573, p.1
- Marsh T.R., Horne K., 1988, MNRAS 235, 269
- McClintock, J.E., Canizares, C.R., & Tarter, C.B. 1975, ApJ, 198, 641
- Muñoz-Darias, T., Casares, J., & Martinez-Pais, I.G. 2005, ApJ, 635, 502
- Nelemans, G., Jonker, P.G., & Steeghs, D. 2006, 370, 255
- O'Donoghue, D., & Charles, P.A. 1996, MNRAS, 282, 191
- Paczynski B. 1974, A&A, 34, 161
- Paczynski, B. 1983, ApJ, 273, L81
- Patterson, J., Kemp, J., Harvey, D.A., Fried, R.E., Rea, R., Monard, B., Cook, L.M., Skillman, D.R., Vanmunster, T., et al. 2005, PASP, 117, 1204
- Pearson, K.J., Hynes, R.I., Steeghs, D., Jonker, P.G., Haswell, C.A., King, A.R., O'Brien, K., Nelemans, G., & Mendez, M. 2006, ApJ, 648, 1169
- Reig P., Papadakis I., Kylafis N.D., 2003, A&A, 398, 1103
- Reynolds, M.T., Callanan, P.J., Filippenko, A.V. 2007, MNRAS, 374, 657
- Scargle, J.D., 1982, ApJ, 263, 835
- Schaefer B.E., 1990, ApJ, 354, 720
- Schenker, K., & King, A.R. 2002, ASP Conf. Ser. 261, The Physics of Cataclysmic Variables and Related Objects, 261, 242
- Schneider D.P., Young P., 1980, ApJ, 238, 946
- Steeghs D., Casares J., 2002, ApJ, 568, 273
- Thorstensen J.R., Ringwald F.A., Wade R.A., Schmidt G.D., & Norsworthy, J.A. 1991, AJ, 102, 272
- Wade R.A., Horne K., 1988, ApJ, 324, 411
- Warner, B. 1995, Ap&SS, 225, 249
- Whitehurst, R. 1988, MNRAS, 232, 35
- Zurita, C., Casares, J., Shahbaz, T., Wagner, R.M., Foltz, C.B., Rodriguez-Gil, P., Hynes, R.I., Charles, P.A., Ryan, E., Schwarz, G., & Starrfield, S.G. 2002, MNRAS, 333, 791

This paper has been typeset from a  $\text{\TeX}$ / $\text{\LaTeX}$  file prepared by the author.